TECTONICS, VOL. 32, 1107–1120, doi:10.1002/tect.20066, 2013

Tectonic implications of fluvial incision and pediment deformation at the northern margin of the Central Anatolian Plateau based on multiple cosmogenic nuclides

Cengiz Yildirim,[1,2,3] Taylor F. Schildgen,[2] Helmut Echtler,[1] Daniel Melnick,[3] Bodo Bookhagen,[3] Attila Çiner,[4] Samuel Niedermann,[1] Silke Merchel,[5] Martin Martschini,[6] Peter Steier,[6] and Manfred R. Strecker[2]

Received 17 November 2012; revised 18 July 2013; accepted 28 July 2013; published 19 September 2013.

[1] We document Quaternary fluvial incision driven by fault-controlled surface deformation in the inverted intermontane Gökırmak Basin in the Central Pontide mountains along the northern margin of the Central Anatolian Plateau. In-situ-produced ^{10}Be, ^{21}Ne, and ^{36}Cl concentrations from gravel-covered fluvial terraces and pediment surfaces along the trunk stream of the basin (the Gökırmak River) yield model exposure ages ranging from 7 ± 1 ka to 346 ± 45 ka and average fluvial incision rates over the past ~350 ka of 0.28 ± 0.01 mm a^{-1}. Similarities between river incision rates and coastal uplift rates at the Black Sea coast suggest that regional uplift is responsible for the river incision. Model exposure ages of deformed pediment surfaces along tributaries of the trunk stream range from 60 ± 5 ka to 110 ± 10 ka, demonstrating that the thrust faults responsible for pediment deformation were active after those times and were likely active earlier as well as explaining the topographic relief of the region. Together, our data demonstrate cumulative incision that is linked to active internal shortening and uplift of ~0.3 mm a^{-1} in the Central Pontide orogenic wedge, which may ultimately contribute to the lateral growth of the northern Anatolian Plateau.

Citation: Yildirim, C., et al. (2013), Tectonic implications of fluvial incision and pediment deformation at the northern margin of the Central Anatolian Plateau based on multiple cosmogenic nuclides, *Tectonics*, *32*, 1107–1120, doi:10.1002/tect.20066.

1. Introduction

[2] The pattern and rate of fluvial incision along major rivers are often useful proxies to reconstruct the history of surface uplift and deformation within a landscape, as fluvial incision typically sets the pace of landscape response to tectonic or climatic forcing [e.g., *Whipple and Meade*, 2004]. Large rivers and their tributaries that have incised bedrock channels in areas such as the Apennines [*Wegmann and Pazzaglia*, 2009], Tibet and the Himalaya [*Hetzel et al*., 2006; *Pan et al*., 2003; *Wobus et al*., 2005; *Kirby and Ouimet*, 2011], and the Andes [*Tosdal et al*., 1984; *Garcia and Hérail*, 2005; *Barke and Lamb*, 2006; *Hoke et al*., 2007; *Schildgen et al*., 2007] have been used as proxies for orogen-scale uplift and regional deformation. In actively deforming regions, planar geomorphic features such as fluvial strath terraces, and pediments are also useful strain markers to quantify deformation related to more localized shortening and uplift along specific structures [*Strecker et al*., 1989; *Benedetti et al*., 2000; *Lavé and Avouac*, 2000].

[3] *Yildirim et al*. [2011] demonstrated that the northern margin of the Central Anatolian plateau (Figures 1a and 1b), defined by the Central Pontide mountains (Figure 1c), is an orogenic wedge with a positive flower-structure geometry between the restraining bend of the North Anatolian Fault (NAF) and the Black Sea (Figure 1d). They further inferred active deformation within the wedge based on deformed Quaternary sediments, GPS-derived slip vectors along the trace of the NAF, and morphometric indices including transient river profiles. Despite this evidence for active deformation, the timing of deformation, its pattern, and the uplift rates have not yet been quantified in the region, making it difficult to assess the importance of the restraining bend of the NAF in terms of long-term topographic development and exhumation along the plateau's northern margin. Fortunately, fluvial terraces and pediments associated with northward-

Additional supporting information may be found in the online version of this article.

[1]İstanbul Technical University, Eurasia Institute of Earth Sciences, Istanbul, Turkey.
[2]Deutsches GeoForschungsZentrum (GFZ), Potsdam, Germany.
[3]Institut für Erd- und Umweltwissenschaften and DFG Leibniz Center for Surface Process and Climate Studies, Universität Potsdam, Potsdam, Germany.
[4]Department of Geography, University of Santa Barbara, Santa Barbara, California, USA.
[5]Department of Geological Engineering, Hacettepe University Ankara, Ankara, Turkey.
[6]Helmholtz-Zentrum Dresden-Rossendorf (HZDR), Dresden, Germany.
[7]Faculty of Physics, Isotope Research, VERA Laboratory, University of Vienna, Vienna, Austria.

Corresponding author: C. Yildirim, İstanbul Technical University, Eurasia Institute of Earth Sciences, Maslak/Sarıyer 34469, Istanbul, Turkey. (cyildirim@itu.edu.tr)

0278-7407/13/10.1002/tect.20066

This article was corrected on 29 NOV 2016. See end of the full text for details.

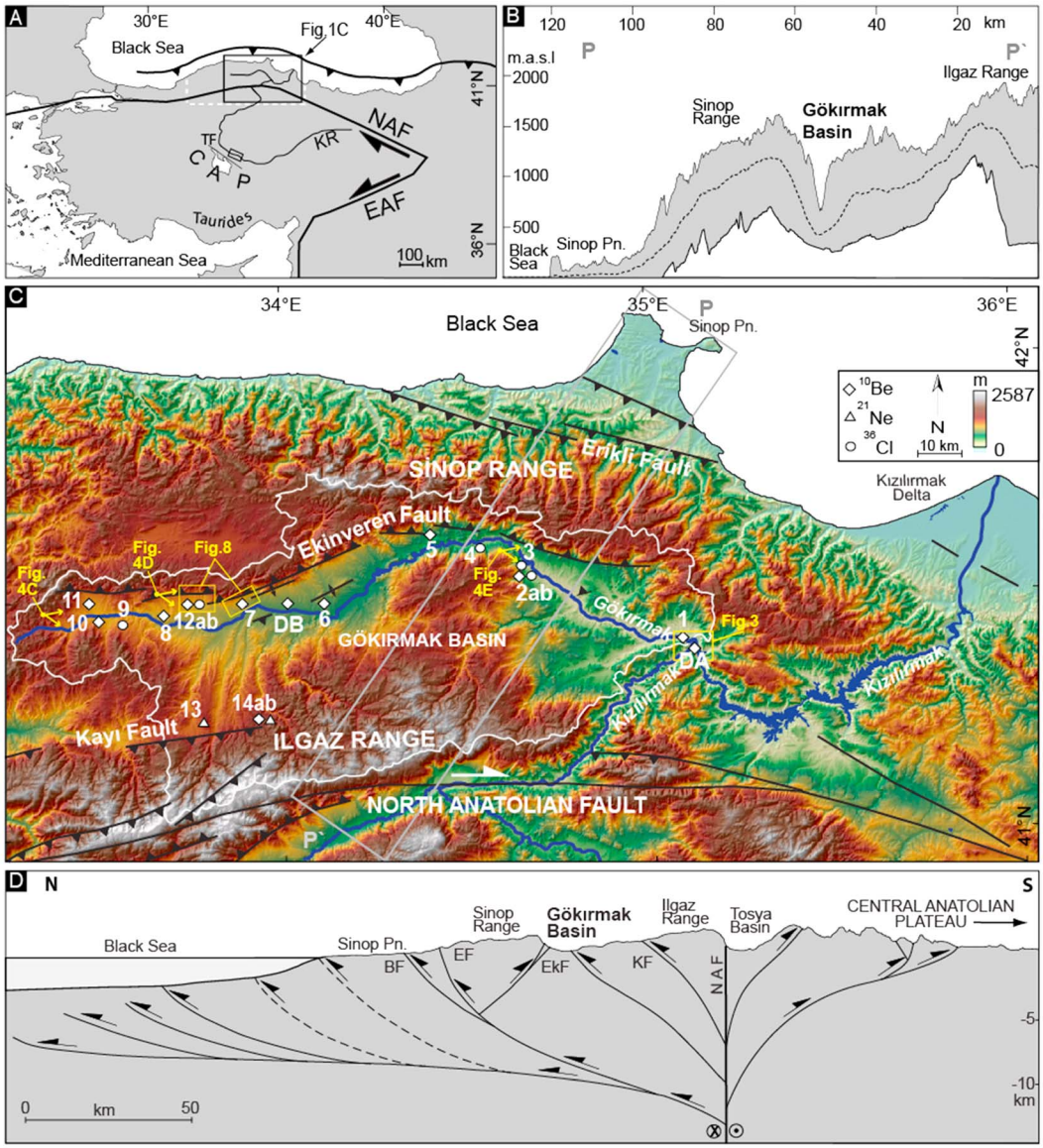

Figure 1. (a) Simplified neotectonic map of Turkey [*Barka and Reilinger*, 1997; *Dilek*, 2006]. CAP: Central Anatolian Plateau, EAF: East Anatolian Fault, KR: Kızılırmak River, NAF: North Anatolian Fault, TF: Tuz Gölü Fault. Dashed white line denotes boundary of the Central Pontides. Small box on the Kızılırmak River shows terrace locations of *Doğan* [2011]. (b) Swath profile of topography across the northern margin of the CAP. The top and bottom of the gray shaded area shows maximum and minimum elevations, respectively. Dashed line shows mean elevation. (c) Topography, active faults [*Şaroğlu et al*., 1992; *Dirik*, 1993; *Andrieux et al*., 1995; *Barka and Reilinger*, 1997; *Şenel*, 2002], drainage system, and morphotectonic units in the study area. Gray box denotes location of the swath profile in Figure 1b. Pn: Peninsula. White line denotes watershed of the Gökırmak Basin. Numbers denote surface samples, and DA and DB show the locations of the depth profiles. Arrows labeled with single capital letters indicate locations and view directions of photos in Figure 2. (d) Conceptual model for the Central Pontides in the form of an active orogenic wedge related to a positive flower structure developed over a shallow detachment surface linked to the North Anatolian Fault at depth (modified after *Yildirim et al*. [2011]). BF: Balıfakı Fault, EF: Erikli Fault, EkF: Ekinveren Fault, KF: Kayı Fault.

flowing rivers sourced from the interior part of the plateau are well suited features to evaluate the rate of regional uplift and patterns of local deformation at the northern plateau margin. Information from the northern margin can then be linked to observations within the central part of the plateau, thus helping to elucidate the characteristics of plateau-margin development on timescales spanning the Quaternary.

[4] In this study, we quantify the rate of late Quaternary fluvial incision in the intermontane Gökırmak Basin in the central part of the Pontide mountains (Figure 1c) by measuring in situ-produced ^{10}Be, ^{21}Ne and ^{36}Cl concentrations

Table 1. Locations, AMS Results, and Model Ages (Inheritance Is Not Corrected) of ^{10}Be Samples

Sample	Latitude (°N)	Longitude (°E)	Elevation (m asl)	Production Rate[a]		Quartz (g)	Be Carrier (mg)	^{10}Be/^{9}Be (x 10^{-13})	^{10}Be Concentration (10^4 atoms/g SiO_2)	^{10}Be Model Age[b] (ka)
				Spallation	Muons					
1	41.4075	35.0941	219	5.03	0.193	98.94	0.20	26.6 ± 7.4	3.5 ± 0.1	7 ± 1
2a	41.5597	34.6714	350	5.65	0.202	114.36	0.20	3900 ± 75	44.6 ± 0.9	81 ± 8
5	41.6314	34.3954	508	6.50	0.213	106.77	0.19	1277 ± 22	15.5 ± 0.3	24 ± 2
6	41.4844	34.1255	618	7.07	0.221	106.34	0.19	2477 ± 47	30.2 ± 0.6	43 ± 4
7	41.4960	33.8898	776	8.08	0.233	100.44	0.20	6465 ± 91	83.9 ± 1.2	110 ± 10
8	41. 4634	33.6730	842	8.51	0.239	113.50	0.20	4317 ± 60	51.2 ± 0.7	178 ± 18
10	41.4674	33.4949	903	8.88	0.243	103.18	0.20	13470 ± 100	170.5 ± 1.3	219 ± 23
11	41.4902	33.4740	902	9.01	0.244	86.08	0.20	14860 ± 310	226.9 ± 4.7	304 ± 34
12a	41.4955	33.7673	882	8.81	0.242	100.00	0.19	4478 ± 72	58.6 ± 0.9	60 ± 5
14a	41.2510	33.9668	1274	11.94	0.275	104.20	0.20	5530 ± 64	69.8 ± 0.8	60 ± 5

[a]Production rates (atoms/g/a) calculated using Lal [1991]/Stone [2000] constant production scaling for surface samples, assuming negligible shielding.
[b]^{10}Be ages were calculated using the Cronus online calculator [*Balco et al*., 2008], assuming no surface denudation. Uncertainties are reported at the 1σ confidence level. ^{10}Be/^{9}Be ratio for standard = 2.85E−12.

(Tables 1–4) on gravel-covered fluvial strath terraces (Figures 2 and 3). The Gökırmak Basin also hosts structures related to young tectonic activity, whose local contributions to deformation we investigate through cosmogenic nuclide exposure dating of deformed pediment surfaces (Figure 4). The area thus allows us to constrain the rate and timing of regional uplift that is related to local deformation along key structures at the northern plateau margin.

2. Regional Tectonic Setting

[5] The northern margin of the Central Anatolian plateau spans the northward-convex Central Pontide mountains between the Black Sea and the curved sector of the North Anatolian Fault (NAF) (Figure 1a). Following closure of the Neotethys Ocean and collision of the Pontide island arc with the Sakarya continent to the south mainly during the late Cretaceous, the Central Pontides were shortened and uplifted along a north-vergent detachment and thin-skinned foreland fold-and-thrust-belt during Paleocene-Eocene time [e.g., *Şengör*, 1995; *Okay and Tüysüz*, 1999; *Dilek*, 2006]. North of the Pontides, the southern Black Sea margin is currently under compression due to collision between Africa-Arabia and Eurasia [*Barka and Reilinger*, 1997; *Cloetingh et al*., 2003]. South of the Pontides, the NAF is the most prominent active member of the dextral North Anatolian Fault Zone [*Şengör et al*., 2005]. The NAF changes strike along its middle portion to form a broad, asymmetric restraining bend (Figure 1a). The Central Pontides are located at the apex and western continuation of this broad bend, where higher contractional strain is likely to be accumulated (Figure 1a). *Yildirim et al*. [2011] found that the NAF-normal component of motion based on GPS-derived slip vectors reaches up to 8 mm a^{-1}. The north-south asymmetric topography of the Central Pontides (Figure 1b) and transient river profiles, combined with the spatial distribution and geometry of Quaternary thrust faults (Figure 1c), imply that the Central Pontides comprise an active orogenic wedge that accommodates NAF-normal contraction on a south-dipping low-angle detachment splaying from the NAF and extending to the Black Sea (Figure 1d) [*Yildirim et al*., 2011].

3. Gökırmak Intermontane Basin

[6] The ~7000 km^2 Gökırmak Basin is the largest intermontane basin within the Central Pontides, with elevations ranging from 170 to 2590 m above sea level (asl) (Figure 1c). The semiarid basin is located in the lee of the coastal ranges and receives an average of 350–500 mm a^{-1} precipitation, which is similar to the central part of the Central Anatolian plateau [*Bozkurt and Sen*, 2011]. The Gökırmak River, which is the main river that drains the Gökırmak Basin, and its tributaries are often flanked by fluvial strath terraces. The straths are covered by 3 to 5 m thick gravel deposits (Figures 2a and 2b), which contain mostly well-rounded pebbles. Their heights vary between 18 and 130 m above the channel (Figure 2c and Tables 5 and 6). The Kızılırmak River is sourced from highlands rising in the eastern part of Anatolia and flows across the Central Anatolian plateau with a crescent-like channel geometry (Figure 1a). The Gökırmak River reaches the Black Sea via the gorge and delta of the Kızılırmak River, approximately 120 km downstream from the study area (Figure 1c). The Kızılırmak gorge is deeply incised, locally very narrow (<100 m) and hosts a series of fluvial terraces and deposits at successively lower elevations (Figures 3a–3d), and steep, landslide-prone slopes and fan delta deposits (Figures 3d and 3e). Along the Black Sea coast, the Kızılırmak delta region is

Table 2. Locations, Cosmogenic ^{21}Ne Concentrations and Model Exposure Ages (Inheritance Is Not Corrected) of Pediment Surfaces Calculated From ^{21}Ne Analyses

Sample	Latitude (°N)	Longitude (°E)	Elevation (m asl)	^{10}Be Production rate (atoms/g/a)	^{21}Ne Production rate[a] (atoms/g/a)	^{21}Ne Concentration[b] (10^4 atoms/g)	Exposure Age[b] (ka)
13	41.2393	33.7869	1130	10.94	48.23	413 ± 23	86 ± 7
14b	41.2510	33.9668	1274	12.22	53.48	372 ± 29	70 ± 7

[a]^{21}Ne production rates were calculated using a value of (0.232 ± 0.009) for the ^{10}Be/^{21}Ne production ratio [*Goethals et al*., 2009].
[b]Uncertainties are reported at the 1σ confidence level.

Table 3. Locations, AMS Results, and Model Ages (Inheritance Is Not Corrected) of ^{36}Cl Samples

Sample	Latitude (°N)	Longitude (°E)	Elevation (m asl)	Production Rate[a] (atoms/(g*a))	^{36}Cl Concentration (10^4 atoms/g)	^{36}Cl Model Age[b] (ka)
2b	41.5597	34.6714	350	69.2	230.6 ± 6.6	133 ± 13
3	41.5780	34.3955	360	70.9	220.4 ± 7.0	118 ± 12
4	41.6140	34.3326	500	78.3	640 ± 12	438 ± 64
9	41.4955	33.4604	931	105.9	460.4 ± 4.6	178 ± 20
12b	41.4955	33.7673	882	109.9	291 ± 10	108 ± 11

[a] ^{36}Cl production rates were calculated using *Stone et al*. [1996] constant production scaling factor with negligible shielding.
[b] ^{36}Cl ages were calculated by using Excel Add-on spreadsheet from *Schimmelpfennig et al*. [2009] assuming no surface denudation. Uncertainties are reported at the 1σ confidence level.

characterized by uplifted Quaternary paleo-deltas at 20 to 30 m and 60 to 70 m asl. [*Akkan*, 1970].

[7] The Gökırmak Basin is bounded to the north by the Sinop range, a push-up structure between the Erikli and Ekinveren thrust faults, and to the south by the Ilgaz range, another push-up structure between the NAF and its transpressional splays (Figures 1c and 1d). The Ekinveren Fault, at the northern margin of the Gökırmak Basin, is the principal structure bounding the mountain front of the Sinop Range (Figure 1c). This N-dipping, E-W striking thrust fault comprises multiple en échelon-segments along the northern flanks of the Gökırmak Basin (Figure 1c) [*Tüysüz*, 1999].

[8] River channels incise through smooth, extensive, low-sloping erosional bedrock surfaces that are mantled by a thin regolith blanket along the mountain fronts of the Gökırmak Basin (Figures 4a–4e). These surfaces are pediments that were sculpted into limestone, marls, and sandstone by erosive processes associated with the transport of the capping regolith [e.g., *Cooke et al*., 1993; *Pelletier*, 2010]. Localized deformation of the pediments has led to incision by the trunk channel or by tributary streams, implying that the surfaces were last active prior to their deformation. The top 1 to 2 m of gravels/regolith capping the higher pediments include well-developed carbonate K-horizons (Figure 4a). The limestone and quartzite clasts are mostly angular and subrounded cobbles or boulders (Figure 4b).

[9] Some of the gently inclined pediment-surface remnants are deformed by active faults and folds along the mountain fronts, leading to different elevations along the southern mountain front compared to those along to northern mountain front. This asymmetry is also reflected by the trunk channel of the basin, which flows closer to the northern mountain front, especially in the central part of the basin (Figure 1c).

4. Methods

4.1. Terrestrial Cosmogenic Nuclide Exposure Dating

[10] The accumulation of in situ-produced terrestrial cosmogenic nuclides [TCNs], such as ^{10}Be, ^{21} Ne, and ^{36}Cl, is related to the time that a fluvial terrace or pediment surface is exposed to secondary cosmic rays and can be used to derive an exposure age for the surface [cf. *Siame et al*., 1997; *Gosse and Phillips*, 2001; *Niedermann*, 2002]. Cosmogenic nuclides are produced in near-surface rocks by neutron-induced spallation, slow (or stopping) muon capture, fast muon-induced reactions, and capture of epithermal and thermal (low-energy) neutrons [*Gosse and Phillips*, 2001, and references therein]. The nuclide ^{10}Be is produced through spallation reactions, stopped negative muon, and fast muon interactions; ^{21}Ne is mainly produced through spallation reactions, and ^{36}Cl is produced through low-energy neutron capture mechanisms, spallation reactions, stopped negative muon, and fast muon interactions [*Zreda et al*., 1991; *Ivy-Ochs and Schaller*, 2009]. Currently, the best-constrained production rates for these nuclides include the production of ^{10}Be and ^{21}Ne in quartz and ^{36}Cl in calcite.

[11] For landforms capped by alluvial or colluvial covers, like river terraces and pediments, exposure ages from TCN concentrations in surface clasts can be complicated by inherited TCNs generated during exhumation and transportation prior to final deposition [*Anderson et al*., 1996; *Hancock et al*., 1999; *Perg et al*., 2001]. Specifically, the measured concentration N in a profile at depth z and time t, assuming uniform inheritance through the profile, can be described by a simplified equation (which can be expanded to include production mechanisms other than spallation):

$$N(z,t) = N_{inher} * e^{-(t/\tau)} + P_{(0)} e^{-\left(z\rho/\Lambda spall\right) * \tau * \left(1 - e^{-(t/\tau)}\right)} \quad (1)$$

Table 4. Locations and AMS Results of ^{10}Be Samples From Depth Profiles DA and DB

Sample	Latitude (°N)	Longitude (°E)	Elevation (m asl)	Depth (cm)	Production Rate[a] Spallation	Production Rate[a] Muons	Quartz (g)	Be Carrier (mg)	^{10}Be/^{9}Be[b] (x 10^{-13})	^{10}Be Concentration[b] (10^4 atoms/g SiO_2)
DA_0	41.3933	35.1170	240	0	5.08	0.194	100.00	0.19862	n/a	n/a
DA_1	41.3933	35.1170		100	1.46	0.168	100.00	0.19330	14.3 ± 0.3	31.6 ± 0.8
DA_2	41.3933	35.1170		200	0.42	0.149	100.00	0.19652	24.4 ± 0.5	18.1 ± 1.4
DB_0	41.4912	33.9836	652	0	7.26	0.224	112.98	0.19690	69.7 ± 1.6	80.0 ± 3.6
DB_1	41.4912	33.9836		120	2.08	0.196	100.00	0.19409	44.8 ± 0.7	57.2 ± 1.8
DB_2	41.4912	33.9836		220	0.6	0.171	100.00	0.19448	12.3 ± 0.2	15.7 ± 0.5

[a] *Lal* [1991]/*Stone* [2000] constant production for surface samples.
[b] Uncertainties are reported at the 1σ confidence level.
We assumed a range of bulk densities (ρ) from 1.6 to 2.0 g cm^{-3} and a neutron-attenuation length (Λ) of 160 g/cm^2 [*Gosse and Phillips*, 2001].

Figure 2. (a) Terrace surface and outcrop of the depth profile DB. (b) Outcrop sampled for depth profile DB. (c) View of terrace staircase. T3 is the terrace surface sampled for sample 4. The rest of the terrace surfaces were not sampled because of anthropogenic impacts on their surfaces. FP: Floodplain.

where N_{inher} is the inheritance at the time of deposition, Λ_{spall} is the attenuation length for spallation-induced reactions, τ is the radioactive mean life, ρ is the density of the material, and $P_{(0)}$ is the production rate at the surface [*Repka et al*., 1997]. Because the production of TCNs by spallation and muon-induced reactions decreases approximately exponentially with depth, deeper samples are effectively shielded from postdepositional accumulation, meaning that measurements of nuclide concentrations from different depths (or one sample at great depth) can be used to estimate the nuclide inheritance in a sedimentary deposit. If that inherited component can be quantified, it can be subtracted from the surface concentration to provide a more reliable exposure age for the surface [*Hancock et al*., 1999].

[12] We collected TCN samples from twelve fluvial strath terraces incised by the Gökırmak River to estimate the timing and rate of regional incision and seven samples from locally deformed pediments associated with active thrusts or folds along the southern and northern mountain fronts to constrain the timing of deformation. We measured ^{10}Be and ^{21}Ne in quartz-rich samples and ^{36}Cl in carbonate samples. Sample sites were selected in areas that had no apparent anthropomorphic modification, away from the edges of the surfaces to minimize postdepositional erosion, and away from surrounding hillslopes to minimize postdepositional burial. On terrace surfaces, we collected at least 30 pebbles with 1 to 3 cm diameter to obtain a representative mean surface concentration [e.g., *Repka et al*., 1997]. At two locations (samples 2a,b and 12a,b), we collected samples of both quartz and carbonate to measure both ^{10}Be and ^{36}Cl, and at one location (sample 14a, b), we measured ^{10}Be and ^{21}Ne nuclides from the same quartz sample to compare exposure ages of the surface derived through different nuclides. We also collected samples along two depth profiles at terrace sites DA and DB (Figures 1c, 2a, 3b, and 3c). For the depth profiles, we similarly collected at least 30 pebbles with 1 to 3 cm diameter at each depth interval so that if there is a grain-size dependence of the inherited nuclide concentration [e.g., *Brown et al*., 1998], our calculated inheritance values from the depth profiles should still be comparable to those of the terrace surface samples. Our samples from the pediment surfaces consist of 5 amalgamated cobbles, to increase the likelihood to get a representative mean surface concentration since the time of pediment abandonment.

4.2. TCN Sample Preparation and Analysis

[13] Chemical preparation of targets for accelerator mass spectrometry (AMS) and quartz samples for noble gas analysis followed variations of established protocols for ^{36}Cl from carbonate [*Stone et al*., 1996; *Conard et al*., 1986] and for ^{10}Be and ^{21}Ne from quartz-rich samples [*Kohl and Nishiizumi*, 1992]. AMS measurements of ^{10}Be were made at Lawrence Livermore National Laboratory. We calculated ^{10}Be surface exposure ages using the CRONUS online calculator version 2.2.1 (available at http://hess.ess.washington.edu/, with documentation in *Balco et al*. [2008]), which includes variations in altitude, latitude, and topographic shielding in calculating production rates from spallation and muons and assumes reference ^{10}Be production rates that depend on the selected scaling scheme (see explanation in the study by *Balco et al*. [2008]). We used the *Lal* [1991]/*Stone* [2000] constant production scaling scheme. Uncertainties in the reference production rates are estimated at ca. 10% [*Balco et al*., 2008]. We rely on the original ICN standard [*Nishiizumi et al*., 2007] and used a ^{10}Be half-life of (1.387 ± 0.012) Ma [*Chmeleff et al*., 2010; *Korschinek et al*., 2010]. Tables 1–3 list the measured

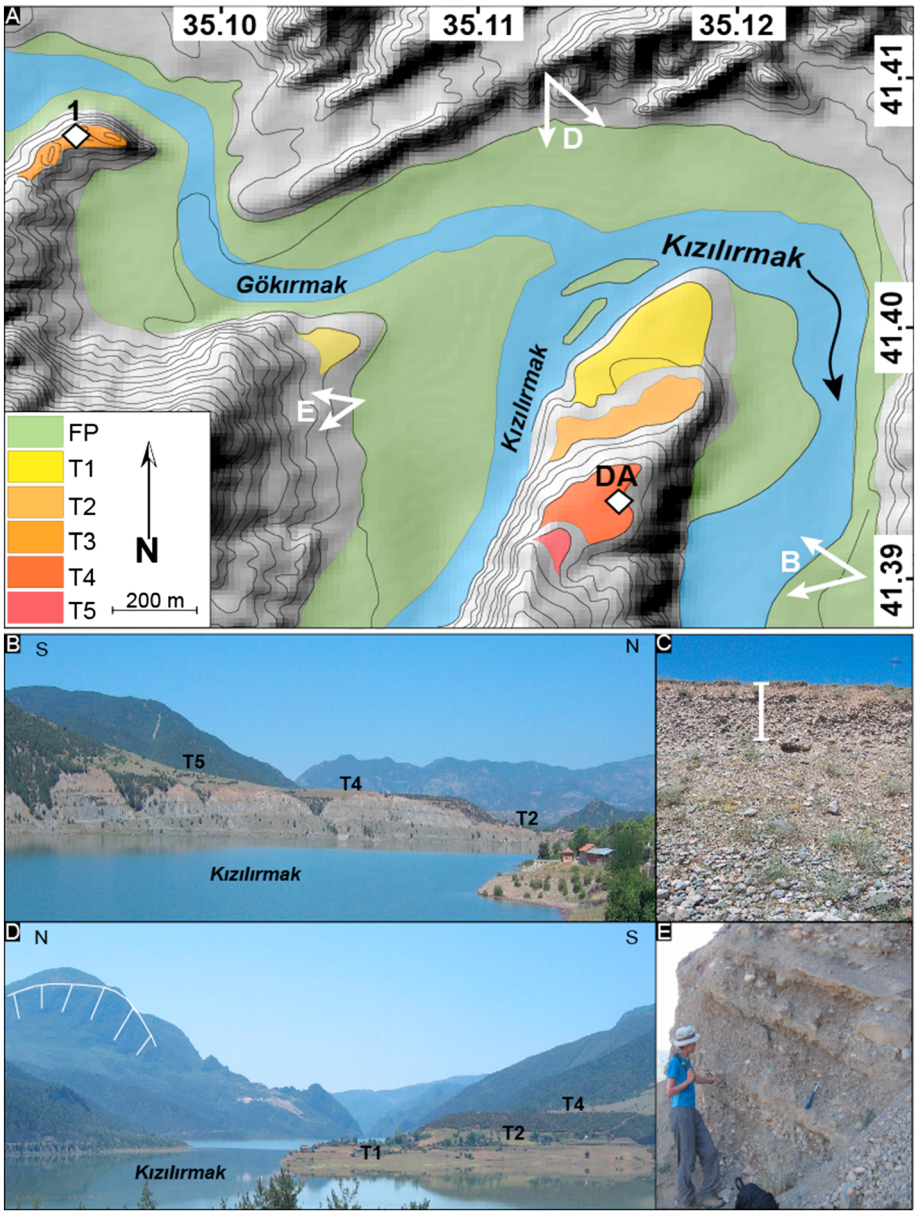

Figure 3. (a) Geomorphological map of the Gökırmak and Kızılırmak confluence. Arrows with capital letters indicate point of views in Figures 3b, 3d, and 3e. FP: Floodplain. (b) River terrace T4 is sampled for depth profile DA. (c) Outcrop sampled for depth profile DA. (d) View of steep, convex slopes of the Kızılırmak Valley at the confluence with the Gökırmak River; white lines show scar of a landslide. (e) Steeply dipping alluvial fan-delta foreset deposits in the Kızılırmak Valley.

^{10}Be, ^{21}Ne and ^{36}Cl concentrations with analytical uncertainties and uncorrected model exposure ages, respectively. To demonstrate the impact of different production rate scaling methods on our results, model exposure ages of ^{10}Be samples based on various scaling schemes are compared in Table S1 in the supporting information.

[14] AMS measurements of ^{36}Cl were performed at the University of Vienna, VERA Laboratory [*Martschini et al.*, 2013] and normalized to SM-Cl-standards [*Merchel et al.*, 2011]. We calculated surface exposure ages using the Excel Add-on provided by *Schimmelpfennig et al.* [2009], which includes variations in altitude, latitude, and topographic shielding in calculating production rates from spallation and muons, and assumes a SLHL ^{36}Cl spallation rate of (48.8 ± 3.4) at g_{Ca}^{-1} a^{-1} [*Stone et al.*, 1996] and a neutron attenuation length of 160 g cm^{-2} [*Gosse and Phillips*, 2001]. Production rates based on the calibration data set of *Stone et al.* [1996] and used for age calculation are based on inductively coupled plasma mass spectrometry (ICP-MS) measurements of major and trace elements of the samples, which are given in Tables S2 and S3 (supporting information), and a ^{36}Cl half-life of 0.301 Ma [*Endt*, 1990].

[15] Two samples (samples 13 and 14b) were analyzed for cosmogenic ^{21}Ne at the facilities of the GFZ Potsdam. The purified quartz was first crushed to a grain size of ~100 µm to open part of the fluid inclusions and thereby reduce the contribution of atmosphere-like trapped Ne. Samples were then wrapped in Al foil and loaded into the sample carrousel

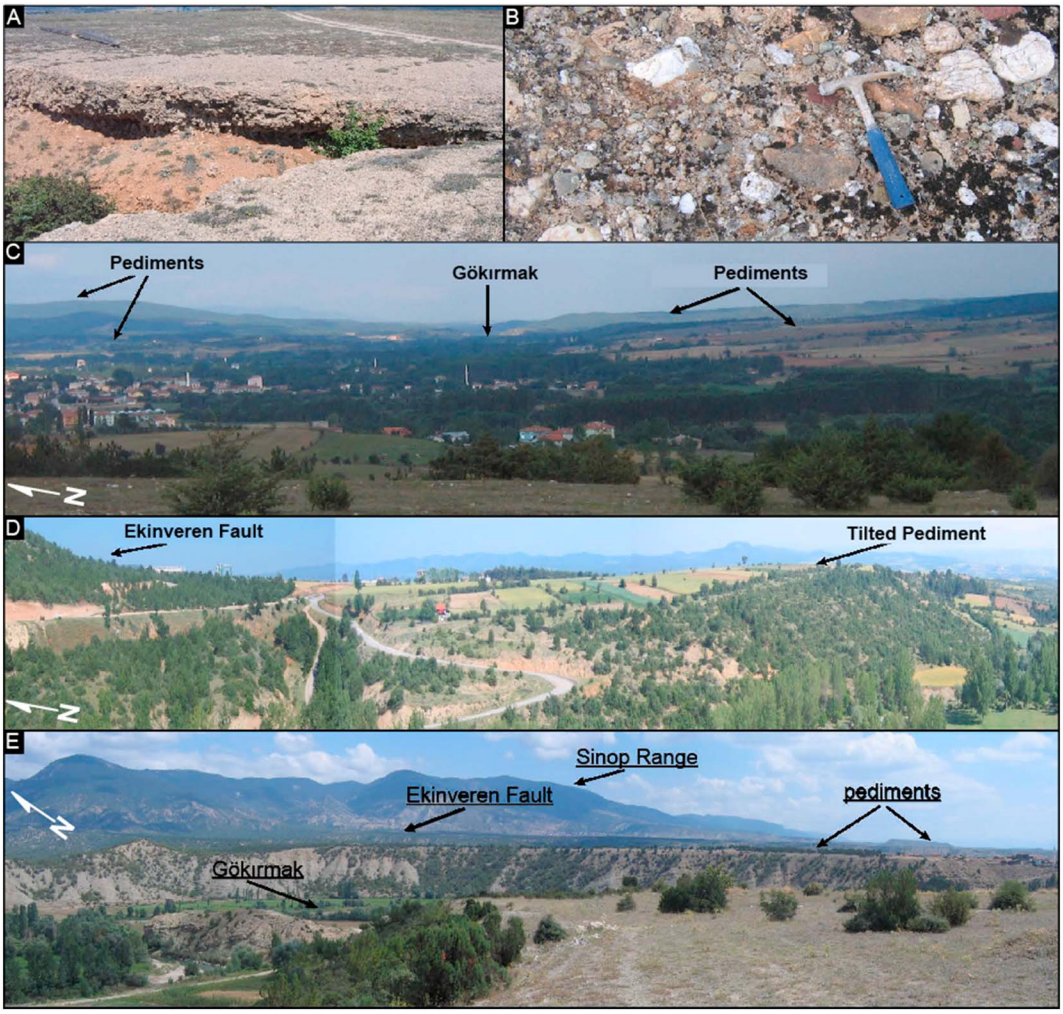

Figure 4. (a) View of a pediment surface and cemented nature of top gravels. (b) Close-up view of cemented pediment surface. (c) View of pediment surface staircases (see Figure 1c for locations of photographs) from the upstream part of the basin. (d) Deformed pediment surface in the midstream part of the basin. The surface is flexed and back tilted toward the mountain front (left) of the Ekinveren Fault. (e) View of pediment surface staircases from the downstream part of the basin.

above the extraction furnace, which was baked at 100°C for about one week. The noble gases were extracted by stepwise heating (at 400, 600, 900, and 1200°C) for 20 min each. In addition, one aliquot of sample 14b was crushed *in vacuo* to check whether trapped Ne was indeed of atmospheric composition. After gas extraction by either heating or crushing, chemically active gases were removed in two Ti sponge and two SAES (ZrAl) getters, and He, Ne, and Ar-Kr-Xe were separated from each other by trapping in a cryogenic adsorber at 11 K and subsequent sequential release. Noble gas concentrations and isotopic compositions were determined in a VG5400 sector field mass spectrometer and were corrected for isobaric interferences, instrumental mass fractionation, and analytical blanks. Further details about the analytical procedures can be found in *Niedermann et al*. [1997].

[16] The crushing extraction yielded a Ne isotopic composition consistent with that of air [$^{22}Ne/^{20}Ne = 0.1020$, $^{21}Ne/^{20}Ne = 0.002959$]; therefore, all ^{21}Ne excesses were calculated relative to atmospheric composition. In the

Table 5. Statistics for the Simulation of the Depth Profiles DA and DB

	Age (ka)	Inheritance (10^4 atoms/g)	Erosion Rate[b] (cm/ka)
DA			
Mean	132.5	10.53	0.11
Median	131.8	10.57	0.11
Mode	130.8	10.36	0.16
Lowest χ^2	142.1	10.41	0.2
Maximum[a]	179.9	14.46	0.26
Minimum[a]	99.9	5.36	0
DB			
Mean	99.3	8.63	0.15
Median	99.2	8.75	0.15
Mode	100.4	9.38	0.26
Lowest χ^2	104.4	10.14	0.24
Maximum[a]	115.0	12.03	0.29
Minimum[a]	84.4	4.10	0

[a]Maximum and minimum values represent the 95% (2σ) confidence window for each parameter.
[b]Maximum total erosion confined to 30 cm.

Table 6. Inheritance Corrected Ages and Incision Rates of the Strath Terraces[a]

Sample	TCN	Height Above River (m)	Age (ka)	Incision Rate (mm/a)
1	^{10}Be	45 ± 5	7 ± 1	6.43 ± 1.16
2a	^{10}Be	30 ± 3	81 ± 8	0.37 ± 0.05
2b	^{36}Cl	30 ± 3	78 ± 7	0.38 ± 0.05
3	^{36}Cl	32 ± 3	68 ± 6	0.47 ± 0.06
4	^{36}Cl	130 ± 10	346 ± 45	0.38 ± 0.06
6	^{10}Be	18 ± 2	43 ± 4	0.42 ± 0.06
DB	^{10}Be	25 ± 3	99 ± 8	0.25 ± 0.04
8	^{10}Be	54 ± 5	178 ± 18	0.30 ± 0.04
10	^{10}Be	52 ± 5	219 ± 23	0.24 ± 0.03
11	^{10}Be	90 ± 9	304 ± 34	0.30 ± 0.04

[a]Uncertainties are reported at the 1σ confidence level.

three-isotope diagram (Figure 5), most data plot on the "spallation line" [*Niedermann et al*., 1993], i.e., they are consistent with a two-component mixture of atmospheric and cosmogenic Ne; some data additionally show a slight isotope fractionation. Excess ^{21}Ne in the 1200°C step is negligible, confirming that the samples do not contain any nucleogenic Ne. Therefore, total cosmogenic ^{21}Ne concentrations were calculated by summing up the ^{21}Ne excesses up to 900°C. We calculated ^{21}Ne production rates using a value of (0.232 ± 0.009) for the ^{10}Be/^{21}Ne production ratio [*Goethals et al*., 2009] to correspond to the ^{10}Be half-life value applied in CRONUS version 2.2.1 [*Balco et al*., 2008], and based on a total ^{10}Be SLHL total production rate derived from the *Lal* [1991]/*Stone* [2000] scaling of the CRONUS online calculator of 4.58 ± 0.43 atoms g^{-1} a^{-1}.

[17] Uncertainties in final reported ages, after the inheritance correction described below, include uncertainties in ^{10}Be and ^{36}Cl production rates, the ^{10}Be/^{21}Ne production ratio, uncertainty in the mass of quartz dissolved, AMS or noble gas mass spectrometric measurements, blank corrections, and Be carrier weighing.

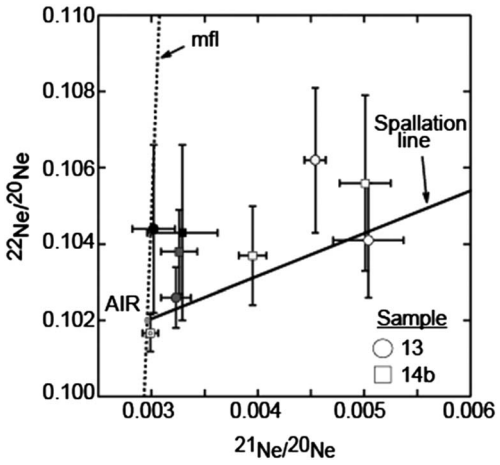

Figure 5. Ne three-isotope diagram for samples 13 and 14b. Light gray symbol with white square inside denotes crusher extraction of sample 14b, white symbols are 400°C, light gray 600°C, dark gray 800°C, and black 1200°C steps. "Spallation line" is the mixing line of atmospheric and cosmogenic Ne according to *Niedermann et al*. [1993]. mfl: mass fractionation line. 2σ uncentertainties are shown.

5. Results

5.1. Nuclide Inheritance and Constraints on Exposure Ages

[18] We determined the ^{10}Be nuclide concentration in depth profiles at two locations (Figure 1c) at road cuts (Figures 2a, 2b, 3b, and 3c) to estimate the nuclide inheritance of our samples, which allows us to calculate a more reliable exposure age from the surface-sample TCN concentrations. Advanced carbonate cementation of the gravels precluded depth-profile sampling at most locations. Table 4 lists ^{10}Be concentrations of the samples from depth profiles. The depth profiles consist of amalgamated quartz clasts from the surface, 1.0 (or 1.2) m, and 2.0 (or 2.2) m depth below the surface at two terraces (Figures 2a, 2b, 3b, and 3c) located at the center and eastern end of the Gökırmak Basin (Figure 1c).

[19] We modeled the ^{10}Be concentration in the two depth profiles (Figures 6a and 6b) by varying the surface age, deposit density, and erosion rate with a Monte Carlo simulator developed by *Hidy et al*. [2010] to calculate the most probable values for inherited nuclide concentration and exposure age. The spallogenic nuclide production is accounted for by using the *Lal* [1991]/*Stone* [2000] constant production scaling model, and the muogenic component of the production rate is accounted for in the simulator by applying the theoretical production equations of *Heisinger et al*. [2002a, 2002b]. The uncertainty in total production rate was estimated to be 10% according to *Balco et al*. [2008]. We explored a range of bulk densities (ρ) (assumed to be uniform throughout

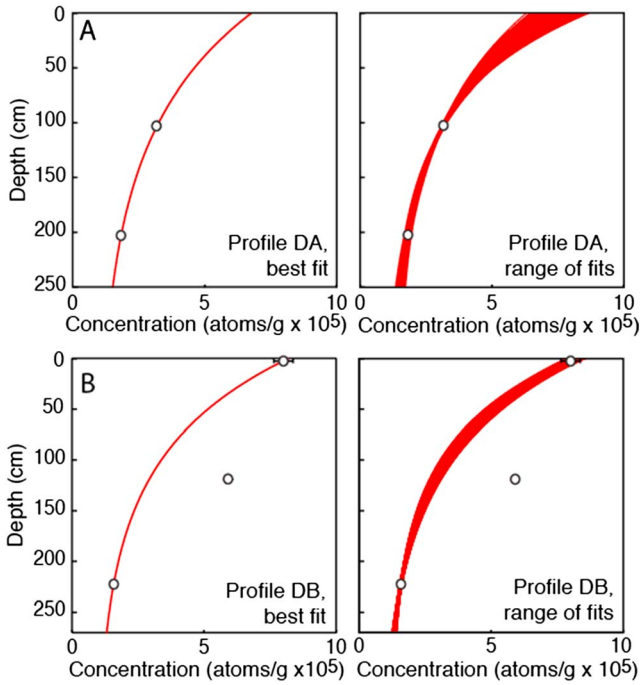

Figure 6. (a) Concentration versus depth plots illustrating the (right) 2σ profile solution spaces and (left) best fits curve for the depth profile DA. (b) Concentration versus depth plots illustrating the (right) 2σ profile solution spaces and (left) best fits curve for the depth profile DB. The 1.2-m depth sample was not part of the simulation due to discordance with the theoretical change in nuclide concentration with depth. Statistics for these simulations are shown in Table 5.

the profile) from 1.6 to 2.0 g cm^{-3}, assumed a neutron-attenuation length (Λ) of 160 g cm^{-2} [*Gosse and Phillips*, 2001], a maximum erosion rate of 1 cm ka^{-1}, and a total erosion of 30 cm. Despite the maximum erosion rate constraint being quite low, the results of the Monte Carlo simulations (summarized in Table 5) demonstrate that the best fit erosion rates are lower than our maximum constraint, which is likely the result of the essentially flat (hence, very slowly eroding) slopes that cap the terraces.

[20] The three samples of depth profile DA were taken from gravels capping a strath terrace at the confluence of the Gökırmak and Kızılırmak rivers (Figures 3a–3c). Unfortunately, the surface sample collected from the depth profile DA was lost during laboratory processing. Although losing the surface sample precludes making a well-constrained estimate of the age of the surface, the two samples at 1.0 and 2.0 m depth still allow us to make a reasonable estimate of the ^{10}Be nuclide inheritance (Figure 6a). The depth-concentration simulation yielded the most probable mean values of 133 +47/-33 ka for the exposure age and (10.5 +4.0/-5.1) × 10^4 atoms g^{-1} for the inherited concentration of ^{10}Be within the gravel deposit (Table 5). Due to the very large error on the modeled age, we do not use the age in any further analysis.

[21] The three samples of depth profile DB were taken from the midstream part of the basin (Figures 1c, 2a, and 2b). The sample from 1.2 m depth shows discordance with the theoretical change in nuclide concentration with depth (Figure 6b). Because we observed no evidence for compositional changes or multistep deposition in the stratigraphy of the gravel, the higher concentration of the 1.2 m depth sample may indicate variable inheritance in the amalgams of heterogeneous clasts [e.g., *Codilean et al*., 2008; *Le Dortz et al*., 2012]. We tested various possibilities to calculate the most probable values for inherited nuclide concentration, exposure age, and erosion rate. The Monte Carlo simulation found no set of parameter values to match the data at a confidence interval lower than 10σ when we included all three samples (from surface and 1.2 m and 2.2 m depths). After discarding the sample at 1.2 m below the surface, the simulation ran well at a 2σ confidence level and yielded the most probable mean values of 99 +16/−15 ka for the age and (8.6 +1.5/−4.5) × 10^4 atoms g^{-1} for the inherited concentration (Figure 6b and Table 5). If we exclude the top sample instead, the model finds no set of parameter values to match the data at a confidence interval lower than 9σ, even when allowing for terrace ages up to 1 Ma. Alternatively, if we exclude the 2.2 m sample, the resulting modeled inherited concentration is ~5 times the inherited concentration derived from depth profile DA and is higher than the concentration of several of the surface samples from other terraces. For these reasons, we believe that the middle sample is the most likely outlier and that it should be excluded when estimating the inherited concentration.

[22] Despite sample site DA being located at the downstream portion of the basin, with a probable contribution from the Kızılırmak River catchment, the inherited concentration calculated from depth profile DA overlaps within error of that calculated from depth profile DB (Table 5). Nonetheless, because the inherited concentration that we obtained from the depth profile DA might contain a signal from the whole Kızılırmak River catchment, including the internal part of the plateau, we preferred to use the inherited concentration that we obtained from the depth profile DB because it reflects inheritance only related to the Gökırmak River catchment. We assume that same inheritance for all fluvial strath terrace surfaces in the catchment.

[23] Because we only measured ^{10}Be in the depth-profile samples, we have no direct measurements of inheritance values for ^{36}Cl samples taken from fluvial strath terrace surfaces. The production mechanisms for ^{36}Cl are different from those for ^{10}Be, therefore, the depth-dependency of production rates differs for the two nuclides. This difference could lead to slight variations in the ratio of the inherited concentration of the two nuclides, particularly if the samples experience any complex exposure histories [*Gosse and Phillips*, 2001]. *Braucher et al*. [2011] measured concentrations of ^{10}Be and ^{36}Cl from a core drilled down to 11 m below the surface and found that ^{36}Cl concentrations between 1 m and 4.3 m depth are consistently around 10 times higher than ^{10}Be concentrations. Although there are numerous ^{36}Cl production pathways and they are strongly dependant on bulk chemical composition, due to the lack of experimental ^{36}Cl data for individual samples at depth from our sampling site, we estimate a rough ^{36}Cl inheritance value by following the observations of *Braucher et al*. [2011] and multiplying our inherited ^{10}Be concentrations (8.6 +1.5/-4.5 x10^4 atoms g^{-1}) by a factor of 10 (the approximate production rate ratio of ^{36}Cl/^{10}Be). It must be noted that, although these corrections to the measured ^{36}Cl concentrations are quite large (therefore, lend greater uncertainty to the final model ^{36}Cl exposure age), they considerably reduce the discrepancy between our ^{10}Be and ^{36}Cl ages (Tables 1 and 3). These results suggest that inheritance corrections are an important component for obtaining accurate ^{36}Cl exposure ages of transported gravels.

5.2. Surface Exposure Ages of the Strath Terraces

[24] Because the surface exposure ages calculated for each sample represents the time elapsed since the respective surface was active gravel transport environments, we consider them to represent "abandonment ages" for the formerly active fluvial channels or pediment surfaces. The surface exposure ages of the fluvial terraces are listed in Table 6. The 10 samples collected from strath terrace surfaces along the trunk channel yield inheritance-corrected model exposure ages that range from 7 ± 1 ka to 346 ± 45 ka (Table 6). The terrace exposure ages generally increase in age with greater height, from 43 ± 4 ka at 18 m above the river (sample 6) to 346 ± 45 ka at 130 m (Figure 3c; sample 4) above the river (Figure 7). One exception is sample 1, which yields a very young age (7 ± 1 ka) for a relatively high terrace (45 m), thus plotting as an outlier from the regional trend (Figure 7).

5.3. Surface Exposure Ages of the Pediment Surfaces

[25] In calculating exposure ages for the pediment surfaces, we did not include inheritance corrections, since our inheritance estimate is derived from fluvial sediments, and the gravels on the pediment surfaces experience a different exhumation and transport history, with potentially long transport times across the pediment surface [e.g., *Nichols et al*., 2005]. For this reason, the surface exposure ages of the pediment surfaces should yield maximum ages for when these surfaces were last active. The three samples from different fragments of a pediment surface that is deformed by the

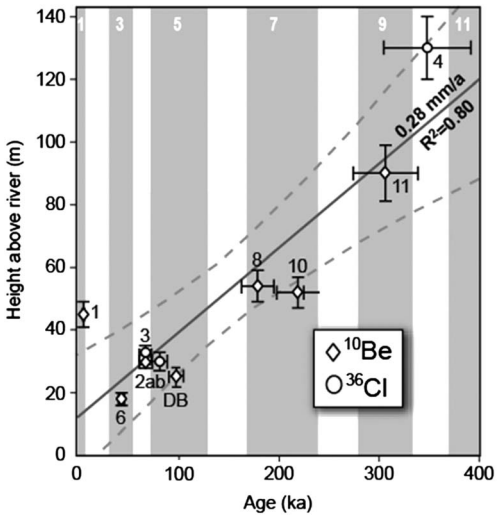

Figure 7. Terrace abandonment ages (based on *Lal* [1991]/*Stone* [2000] scaling; Table 6) versus heights above the river. Bars on symbols show 1σ uncertainties. Odd-numbered MIS are highlighted with white colored numbers and dark gray shading. Black numbers are numbers of samples. Bold line is the median regression line of ^{10}Be and ^{36}Cl ages versus elevation, while dashed thick dark gray lines represent the 95% confidence intervals based on n = 1000 bootstrap simulations of an ordinary least squares regression.

Kayı Fault along the southern mountain front (samples 13, 14a, and 14b; Figure 1c) yield exposure ages of 86 ± 7 ka and 70 ± 7 ka from ^{21}Ne analyses, and 60 ± 5 ka from ^{10}Be analyses (Tables 1 and 2). The other three samples analyzed for ^{10}Be (samples 7 and 12a) and ^{36}Cl (sample 12b) from different pediment surfaces deformed by the Ekinveren Fault (Figures 8a and 8b) and a frontal fold along the northern mountain front (Figure 8c) yield ages of 110 ± 10 ka, 60 ± 5 ka and 108 ± 11 ka, respectively (Tables 1, 3, and 7). The maximum ages of the surfaces demonstrate Quaternary (and possibly earlier) activity of faults and folds within the basin.

5.4. River Incision Rates From Strath Terraces

[26] To calculate river-incision rates based on an individual fluvial strath terrace, we divide the terrace height by its inheritance-corrected exposure (abandonment) age. The individual terraces yield incision rates ranging from 0.24 to 6.43 mm/a (Table 6).

[27] To calculate mean incision rates based on all of the fluvial strath terraces along the trunk stream of the Gökırmak River, we used a boot-strapped ordinary least squares regression of the relationship between terrace heights above the river and the inheritance-corrected abandonment ages. To quantify potential uncertainties brought about by propagating both field and laboratory measurement errors (including the effect of potential outliers), we replicated n = 1000 data subsets from (a) ^{10}Be and (b) ^{36}Cl by randomly drawing with replacement each data point from a normal distribution according to the means and standard deviations specified by the AMS measurements. We then calculated an ordinary least squares model for each of these 1000 boot-strap data subsets and estimated the probability density functions (pdfs) of the resulting regression slopes. We used both the original and centered data to account for the effect of a fixed intercept $t = 0$ (see Table S4 in the supporting information for summary). From these pdfs, we derived the medians and the 95% confidence intervals. We skipped T-tests to

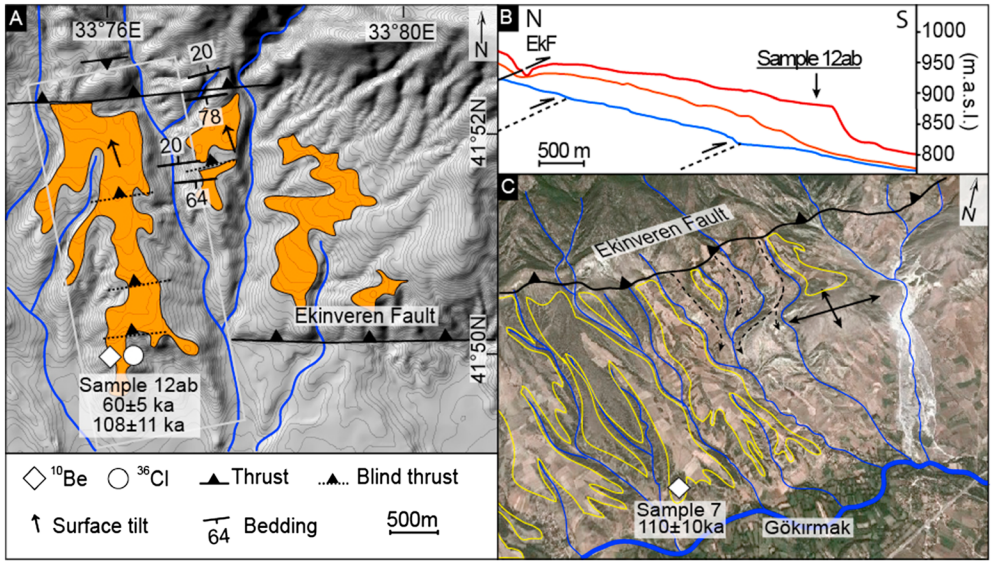

Figure 8. (a) Map view of deformed pediment surface of sample 12ab; bedding planes from Quaternary lacustrine limestone. Contour interval is 5 m. Orange polygons represent the pediment surfaces. (b) Swath profile (light gray outlined box in Figure 8a) showing tilting of pediment surface and knickpoints along channel as a result of fault propagation toward the south. Red, orange, and blue lines indicate maximum, mean, and minimum elevations, respectively. EkF: Ekinveren Fault. (c) Oblique view of deformed pediment surface of the sample 7. Dashed lines with arrows indicate interfluves of channels deflected as a result of fold propagation toward west. Yellow lines outline the pediment boundaries.

Table 7. Surface Exposure Ages of the Pediment Surfaces[a]

Sample	TCN	Age (ka)
5	^{10}Be	24 ± 2
7	^{10}Be	110 ± 10
9	^{36}Cl	178 ± 20
12a	^{10}Be	60 ± 5
12b	^{36}Cl	108 ± 11
13	^{21}Ne	86 ± 7
14a	^{10}Be	60 ± 5
14b	^{21}Ne	70 ± 7

[a]Uncertainties are reported at the 1σ confidence level.

check for significant differences between the different models, as the inferred incision rates are rather well constrained to 0.27–0.29 mm a^{-1} (Figure 7).

6. Discussion

6.1. Tectonic and Climatic Controls on Fluvial Terrace Formation

[28] Fluvial incision or aggradation may result from tectonic, climate, or other local factors. These effects may include uplift or subsidence, climatically driven base-level changes, changes in discharge, changes in sediment load, and stream capture [e.g., *Schumm*, 1977; *Hancock and Anderson*, 2002; *Vandenberghe*, 2003; *Bookhagen and Strecker*, 2012]. Nonetheless, the staircase morphology of fluvial strath terraces only forms in regions where long-term uplift raises older abandoned surfaces to progressively higher elevations [e.g., *Bridgland*, 2000; *Maddy et al*., 2001; *Westaway et al*., 2004; *Wegmann and Pazzaglia*, 2009; *Schildgen et al*., 2012]. Because climate-related changes in sediment load and discharge tend to occur in cycles, particularly glacial-interglacial cycles, fluvial incision applied as a proxy for uplift should integrate over at least one glacial-interglacial cycle [*Hancock and Anderson*, 2002; *Wegmann and Pazzaglia*, 2002].

[29] *Doğan* [2011] suggested that terrace formation along the Kızılırmak River in the central part of the Central Anatolian plateau was forced by orbital cycles and that the main terrace abandonment phases occurred during glacial periods. Although a number of other studies have also demonstrated correlations between MIS stages and terrace formation times in other regions [e.g., *Benedetti et al*., 2000; *Pazzaglia and Brandon*, 2001; *Schildgen et al*., 2012], the ages from the Gökırmak Basin (even considering the nontrivial errors) show a variable relationship with glacial and interglacial stages (Figure 7). This difference in the timing of terrace abandonment between the central part of the plateau and its northern margin suggests that variations in sediment flux and/or discharge resulting from glacial-interglacial cycles are not the only factor that controls the change between lateral and vertical river incision in the Gökırmak Basin. Rather, the Gökırmak Basin might experience vertical uplift rates that vary on the time scale of individual terrace formation, or other minor climate cycles could influence the formation of terraces in that region. Currently, however, no high-resolution uplift-rate estimates allow us to test this possibility further.

6.2. Local Influences on Incision Record

[30] Stream capture is a geomorphic phenomenon that may trigger and/or accelerate incision due to additional discharge obtained from captured streams or water bodies. This process is particularly important to consider along major strike-slip fault systems, where lateral motions through time may cause downstream river segments to capture larger or smaller drainage areas on the opposite side of the fault [e.g., *Hubert-Ferrari et al*., 2002] and subsequently lead to aggradation or incision as the new channel adjusts to its new length and drainage area. *Hubert-Ferrari et al*. [2002] and *Şengör et al*. [2005] proposed that the Kızılırmak River established its present course across the NAF and to its outlet at the Black Sea at ca. 2 Ma. Prior to that time, the modern headwaters of the Kızılırmak River appear to have been internally drained [*Ardel*, 1967]. Because the Gökırmak Basin drains into the lower part of the Kızılırmak River between the NAF and the Black Sea, it must have experienced any changes in the elevation of its outlet to the Kızılırmak River at approximately the same period of time. The presence of incised lacustrine deposits within the subbasins of the Gökırmak Basin that are connected with each other via deep gorges could have resulted from such transient adjustments following the establishment of the modern Kızılırmak channel. Nonetheless, the ~2 Ma estimate for the timing of the capture of the Kızılırmak headwaters is much earlier than our oldest terrace abandonment age of 346 ka, implying that the incision recorded in the Gökırmak Basin since 346 ka is not likely associated with capture-related processes.

[31] Although we rule out effects of stream capture as an important influence on the incision record, other local effects may have been significant, particularly along the very narrow valleys of the Kızılırmak River (Figure 3d). For example, recent processes such as landsliding and/or rapidly changing sediment loads within the Kızılırmak Valley may have led to temporary blocking/damming and reincision of the Gökırmak Valley. The alluvial-fan delta deposits (Figure 3e) that we observed on the upstream side of landslides at the outlet of the Gökırmak Basin indicate that a paleo-fan delta was deposited in a water body that was probably dammed at the Kızılırmak Valley. The very young exposure age (~7 ka) and high incision rate (6.43 mm a^{-1}) that we obtained from a strath terrace at the outlet of the Gökirmak Basin might be related to either shielding of the terrace surface from cosmic rays as a result of such damming and subsequent reincision of the gorge or from the creation of a new epigenetic gorge if the river incised through the bedrock in a different location compared to the earlier valley [e.g., *Ouimet et al*., 2008]. For that reason, we excluded that sample when performing the boot-strap regression to determine the mean regional incision rate.

6.3. Deformed Pediment Surfaces and Regional Patterns of Crustal Deformation

[32] Pediment surfaces are generally smooth and gentle surfaces inclined toward the basin. They are geomorphic markers of the base-level stabilities across the northern margin. The presence of the deformed pediment surfaces (Figures 8a and 8b) along the Ekinveren Fault indicate upper crustal shortening in the Central Pontide wedge related to thrust faults. Our TCN data from deformed pediment surfaces (Figures 8a and 8b) reveal that thrust faulting continued at least through Late Quaternary time.

[33] This deformation is not only restricted to the Gökırmak Basin but extends across the array of ranges between the NAF and the Black Sea (Figure 1d). Seismic reflection profiles

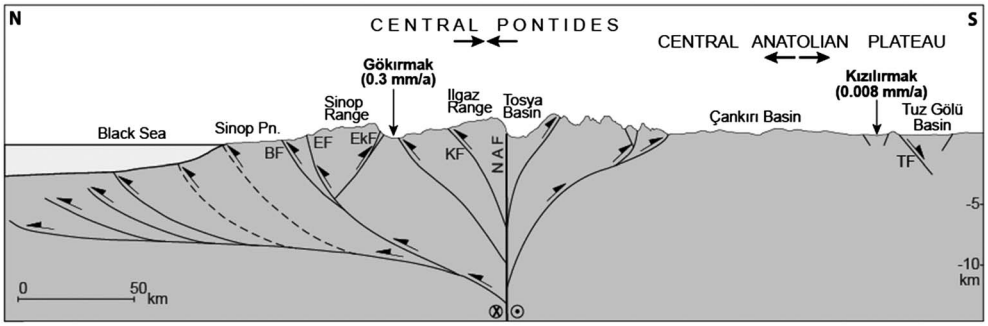

Figure 9. Cross section illustrating conceptual model for the Central Pontides in the form of an active orogenic wedge (modified after *Yildirim et al*. [2011]) together with river incision rates from the interior part of the Central Anatolian Plateau (from *Doğan* [2011]) and from the Gökırmak Basin. BF: Balıfakı Fault, EF: Erikli Fault, EkF: Ekinveren Fault, KF: Kayı Fault, NAF: North Anatolian Fault, TF: Tuz Gölü Fault. Arrows indicate shortening in the Pontides and extension in the Central Anatolian Plateau.

[*Finetti et al*., 1988] combined with morphometric data [*Yildirim et al*., 2011] show hinterland propagation of the deformation by out-of-sequence faulting, implying that upper-crustal shortening takes place on faults spanning the width of the wedge. The out-of-sequence nature of deformation is underscored by undeformed Pliocene and Quaternary sediments covering the outermost thrust front [*Finetti et al*., 1988].

[34] According to wedge theory, an orogenic wedge will advance toward its foreland and lengthen itself when the sum of its basal and upper slopes exceeds a critical taper value; conversely, if the sum of the slopes is less than the critical value, internal shortening will thicken the wedge and build topography until it reaches the critical taper [*Dahlen*, 1990; *Mitra*, 1997; *DeCelles and Mitra*, 1995]. Especially after focused erosion reduces topographic slope and drives the wedge into a "subcritical" state, the wedge may attempt to regain taper through out-of-sequence thrusting or duplexing before propagating outward [*Dahlen*, 1990]. Given our new evidence for ongoing out-of-sequence deformation in the Central Pontides and the inferred subcritical state of the orogenic wedge, we conclude that the Central Pontides are currently in a state of rebuilding topography that may have been lost earlier through basin exhumation and spatially focused erosion.

[35] Finally, with respect to the overall evolution of the Central Anatolia Plateau, our observations of uplifted and deformed geomorphic reference horizons unambiguously show that the lateral growth of the plateau has continued into the Quaternary and is ongoing. Continued vertical growth of the interior part of the wedge may ultimately result in continued northward orogenic growth and possible reactivation of thrust systems at the periphery of the Pontide wedge.

6.4. Differential Uplift Between the Northern Margin and the Central Part of the Plateau

[36] Even in the absence of local influences on the incision record, the mean fluvial incision rate does not always match the mean uplift rate in actively deforming areas, particularly if fluvial response times are slow, as may happen in the upper reaches of a large river catchment. Because no significant knickpoints occur between our terrace locations and the river outlet, the river incision rate should be adjusted to recent uplift rates [e.g., *Whipple and Meade*, 2004], implying that our mean incision rate derived from fluvial strath terraces reflects the mean uplift rate in the Gökırmak Basin. Also, uplifted Quaternary paleo-deltas of the Kızılırmak River, 120 km downstream from the outlet of the Gökırmak Basin, yield an inferred uplift rate of 0.2–0.3 mm a^{-1} during the last 346 ka based on correlations between delta formation and relative sea level highstands [*Demir et al*., 2004]. The similarity between this coastal uplift rate and our 0.27–0.29 mm a^{-1} mean incision rate along the trunk stream of the Gökırmak Basin over the last 346 ka (Figure 7) further supports our inference that the mean incision rate reflects the mean uplift rate along the northern margin of the Central Anatolian Plateau over the past ~350 ka.

[37] In contrast to the correspondence between our incision rates from the northern plateau margin and uplift rates along the coast, river terraces along the Kızılırmak River in the central part of the plateau (Figure 1a) record an incision rate that is three times lower, i.e., 0.08 mm a^{-1} averaged over the last 400 ka (Figure 9) [*Doğan*, 2011]. This difference between the central part of the plateau and its northern margin indicates that either the northward-flowing Kızılırmak River is currently in a transient state, with portions of the river upstream from the Gökırmak Basin not yet adjusted to the faster recent uplift rates or that faster uplift has occurred at least since the Late Pleistocene time along the northern margin of the plateau compared to the central region. Without independent estimates of the uplift rate in the central plateau region, we cannot currently discriminate between these two possibilities.

7. Conclusions

[38] Despite potential complexities involving climate cycles and local river incision processes, the patterns of deformation and rates of river incision in the Gökırmak Basin support the notion that active deformation and uplift are the primary factors driving fluvial incision of the northern margin of the Central Anatolian plateau. Terrestrial cosmogenic nuclide-derived abandonment ages of fluvial strath terraces along the trunk channel of the Gökırmak River imply that long-term average incision rates over the past ~350 ka were 0.27–0.29 mm a^{-1}. Surface exposure ages of deformed pediment surfaces ranging from ~60 to 110 ka demonstrate that thrust faults responsible for the pediment deformation have been active at least since that time and were likely active much earlier as well to explain the amount of topographic

relief in the region. Any inference about earlier activity, however, implies that the pediments formed during a relatively recent phase of base level stability and/or tectonic quiescence. Because the average incision along the Gökırmak River matches uplift rates inferred for deltaic deposits at the coast, and because the deformed pediment surfaces correspond to locations above thrust faults, we interpret incision within the Gökırmak Basin to be driven primarily by differential uplift through thrusting. This active shortening, coupled with a regional out-of-sequence faulting pattern, implies that the Central Pontides orogenic wedge is actively growing by internal shortening.

[39] **Acknowledgments.** This work is part of the Vertical Anatolian Movements Project, funded by the TOPO-EUROPE initiative of the European Science Foundation, including contributions by the German Science Foundation (DFG) to MS (grants STR373/20-1 and 25-1). CY was supported by Potsdam University and Deutsches GeoForschungsZentrum Potsdam; HE was supported by DFG. TS was supported by the Leibniz Center for Surface Processes and Climate Studies at the University of Potsdam (DFG: STR373/20-1) and the Alexander von Humboldt Foundation. BB was supported with grants from NASA (NNX08AG05G), AC was supported by TÜBITAK (107Y333). We thank E. Schnabel for performing noble gas analyses; A. Musiol, K. Hahne, and H. Rothe for major and trace element measurements; A. Landgraf, I. Schimmelpfennig, and A. Hidy for discussions on cosmogenic nuclides and depth profiles; B. Rojay, U. Doğan, P. Ballato, S. Hoth, and C. Kunze for discussions of regional geology and geomorphology; and Y. Garcin and O. Korup for help with the statistical analysis and discussions.

References

Akkan, E. (1970), Bafra burnu-Delice kavsağı arasında Kızılırmak vadisinin jeomorfolojisi: *Ankara. Üniversitesi. Dil, Tarih, Coğ. Fak. Yayınları, 191*, p. 158.

Anderson, R. S., J. L. Repka, and G. S. Dick (1996), Explicit treatment of inheritance in dating depositional surfaces using in situ 10Be and 26Al, *Geology*, *24*(1), 47–51.

Andrieux, J., S. Över, A. Poisson, and O. Bellier (1995), The North Anatolian fault zone distributed neogene deformation in its northward convex part, *Tectonophysics*, *243*(1–2), 135–154.

Ardel, A. (1967), İç Anadolu Kızılırmak Yayı içinde kalan sahada coğrafi müsahadeler, *İstanbul Univ. Coğraf. Enst. Derg.*, *8*, 9–17.

Balco, G., J. O. Stone, N. A. Lifton, and T. J. Dunai (2008), A complete and easily accessible means of calculating surface exposure ages or erosion rates from ^{10}Be and ^{26}Al measurements, *Quat. Geochronol.*, *3*(3), 174–195.

Barka, A., and R. Reilinger (1997), Active tectonics of the Eastern Mediterranean region: Deduced from GPS, neotectonic and seismicity data, *Ann.Geofis.*, *XL*, 587–610.

Barke, R., and S. Lamb (2006), Late Cenozoic uplift of the Eastern Cordillera, Bolivian Andes, *Earth Planet. Sci. Lett.*, *249*(3–4), 350–367.

Benedetti, L., P. Tapponnier, G. C. P. King, B. Meyer, and I. Manighetti (2000), Growth folding and active thrusting in the Montello region, Veneto, northern Italy, *J. Geophys. Res.*, *105*(B1), 739–766.

Bookhagen, B., and M. R. Strecker (2012), Spatiotemporal trends in erosion rates across a pronounced rainfall gradient: Examples from the southern Central Andes, *Earth Planet. Sci. Lett.*, *327–328*, 97–110.

Bozkurt, D., and O. Sen (2011), Precipitation in the Anatolian Peninsula: Sensitivity to increased SSTs in the surrounding seas, *Clim. Dyn.*, *36*(3–4), 711–726.

Braucher, R., S. Merchel, J. Borgomano, and D. L. Bourlès (2011), Production of cosmogenic radionuclides at great depth: A multi element approach, *Earth Planet. Sci. Lett.*, *309*(1–2), 1–9.

Bridgland, D. R. (2000), River terrace systems in north-west Europe: An archive of environmental change, uplift and early human occupation, *Quat. Sci. Rev.*, *19*(13), 1293–1303.

Brown, E. T., R. F. Stallard, M. C. Larsen, D. L. Bourlès, G. M. Raisbeck, and F. Yiou (1998), Determination of predevelopment denudation rates of an agricultural watershed (Cayaguás River, Puerto Rico) using in-situ-produced ^{10}Be in river-borne quartz, *Earth Planet. Sci. Lett.*, *160*(3–4), 723–728.

Chmeleff, J., F. von Blanckenburg, K. Kossert, and D. Jakob (2010), Determination of the ^{10}Be half-life by multicollector ICP-MS and liquid scintillation counting, *Nucl. Instrum. Methods Phys. Res. B*, *268*(2), 192–199.

Cloetingh, S., G. Spadini, J. D. Van Wees, and F. Beekman (2003), Thermomechanical modelling of Black Sea Basin (de)formation, *Sediment. Geol.*, *156*(1–4), 169–184.

Codilean, A. T., P. Bishop, F. M. Stuart, T. B. Hoey, D. Fabel, and S. P. H. T. Freeman (2008), Single-grain cosmogenic Ne-21 concentrations in fluvial sediments reveal spatially variable erosion rates, *Geology*, *36*(2), 159–162.

Conard, N. J., D. Elmore, P. W. Kubik, H. E. Gove, L. E. Tubbs, B. A. Chrunyk, and M. Wahlen (1986), The chemical preparation of AgCl for measuring ^{36}Cl in polar ice with accelerator mass spectrometry, *Radiocarbon*, *28*(2A), 556–560.

Cooke, R. U., A. Warren, and A. Goudie (1993), *Desert Geomorphology*, 526 pp., UCL Press, London.

Dahlen, F. A. (1990), Critical Taper Model of Fold-And-Thrust Belts and Accretionary Wedges, *Annu. Rev. Earth Planet. Sci.*, *18*(1), 55–99.

DeCelles, P. G., and G. Mitra (1995), History of the Sevier orogenic wedge in terms of critical taper models, northeast Utah and southwest Wyoming, *Geol. Soc. Am. Bull.*, *107*, 454–462.

Demir, T., I. Yesilnacar, and R. Westaway (2004), River terrace sequences in Turkey: Sources of evidence for lateral variations in regional uplift, *Proc. Geol. Assoc.*, *115*(4), 289–311.

Dilek, Y. (2006), Collision tectonics of the Mediterranean region: Causes and consequences, *Geol. Soc. Am. Spec. Pap.*, *409*, 1–13.

Dirik, K. (1993), Geological history of the northward arched segment of the North Anatolia Transform Fault Zone, *Geol. J.*, *28*, 251–66.

Doğan, U. (2011), Climate-controlled river terrace formation in the Kızılırmak Valley, Cappadocia section, Turkey: Inferred from Ar-Ar dating of Quaternary basalts and terraces stratigraphy, *Geomorphology*, *126*(1-2), 66–81.

Endt, P. M. (1990), Energy levels of A = 21–44 nuclei (VII), *Nucl. Phys. A.*, *521*, 1–400.

Finetti, I., G. Bricchi, A. M. Del Ben, M. Pipan, and Z. Xuan (1988), Geophysical study of the Black Sea area, *Boll. Geofis. Teor. Appl.*, *30*, 197–324.

Garcia, M., and G. Hérail (2005), Fault-related folding, drainage network evolution and valley incision during the Neogene in the Andean Precordillera of Northern Chile, *Geomorphology*, *65*(3–4), 279–300.

Goethals, M. M., R. Hetzel, S. Niedermann, H. Wittmann, C. R. Fenton, P. W. Kubik, M. Christl, and F. von Blanckenburg (2009), An improved experimental determination of cosmogenic ^{10}Be/^{21}Ne and ^{26}Al/^{21}Ne production ratios in quartz, *Earth Planet. Sci. Lett.*, *284*(1–2), 187–198.

Gosse, J. C., and F. M. Phillips (2001), Terrestrial in situ cosmogenic nuclides: theory and application, *Quat. Sci. Rev.*, *20*(14), 1475–1560.

Hancock, G. S., and R. S. Anderson (2002), Numerical modeling of fluvial strath-terrace formation in response to oscillating climate, *Geol. Soc. Am. Bull.*, *114*(9), 1131–1142.

Hancock, G. S., R. S. Anderson, O. A. Chadwick, and R. C. Finkel (1999), Dating fluvial terraces with ^{10}Be and ^{26}Al profiles: Application to the Wind River, Wyoming, *Geomorphology*, *27*(1–2), 41–60.

Heisinger, B., D. Lal, A. J. T. Jull, P. Kubik, S. Ivy-Ochs, K. Knie, and E. Nolte (2002a), Production of selected cosmogenic radionuclides by muons: 2. Capture of negative muons, *Earth Planet. Sci. Lett.*, *200*(3–4), 357–369.

Heisinger, B., D. Lal, A. J. T. Jull, P. Kubik, S. Ivy-Ochs, S. Neumaier, K. Knie, V. Lazarev, and E. Nolte (2002b), Production of selected cosmogenic radionuclides by muons: 1. Fast muons, *Earth Planet. Sci. Lett.*, *200*(3–4), 345–355.

Hetzel, R., S. Niedermann, M. Tao, P. W. Kubik, and M. R. Strecker (2006), Climatic versus tectonic control on river incision at the margin of NE Tibet: ^{10}Be exposure dating of river terraces at the mountain front of the Qilian Shan, *J. Geophys. Res.*, *111*, F03012, doi:10.1029/2005JF000352.

Hidy, A. J., J. C. Gosse, J. L. Pederson, J. P. Mattern, and R. C. Finkel (2010), A geologically constrained Monte Carlo approach to modeling exposure ages from profiles of cosmogenic nuclides: An example from Lees Ferry, Arizona, *Geochem. Geophys. Geosyst.*, *11*, Q0AA10, doi:10.1029/2010GC003084.

Hoke, G. D., B. L. Isacks, T. E. Jordan, N. Blanco, A. J. Tomlinson, and J. Ramezani (2007), Geomorphic evidence for post-10 Ma uplift of the western flank of the central Andes 18°30'S–22°S, *Tectonics*, *26*, TC5021, doi:10.1029/2006TC002082.

Hubert-Ferrari, A., R. Armijo, G. King, B. Meyer, and A. Barka (2002), Morphology, displacement, and slip rates along the North Anatolian Fault, Turkey, *J. Geophys. Res.*, *107*(B10), 2235, doi:10.1029/2001JB000393.

Ivy-Ochs, S., and M. Schaller (2009), Examining processes and rates of landscape change with cosmogenic radionuclides, in *Radioactivity in the Environment*, Chap. 6, edited by F. Klaus, pp. 231–294, Elsevier, Amsterdam.

Kirby, E., and W. Ouimet (2011), Tectonic geomorphology along the eastern margin of Tibet: Insights into the pattern and processes of active deformation adjacent to the Sichuan Basin, *Geol. Soc. London, Spec. Publ. 353*(1), 165–188.

Kohl, C. P., and K. Nishiizumi (1992), Chemical isolation of quartz for measurement of in-situ -produced cosmogenic nuclides, *Geochim. Cosmochim. Acta*, *56*(9), 3583–3587.

Korschinek, G., et al. (2010), A new value for the half-life of ^{10}Be by Heavy-Ion Elastic Recoil Detection and liquid scintillation counting, *Nucl. Instrum. Methods Phys. Res.*, *268*(2), 187–191.

Lal, D. (1991), Cosmic ray labeling of erosion surfaces: in situ nuclide production rates and erosion models, *Earth Planet. Sci. Lett.*, *104*(2–4), 424–439.

Lavé, J., and J. P. Avouac (2000), Active folding of fluvial terraces across the Siwaliks Hills, Himalayas of central Nepal, *J. Geophys. Res.*, *105*(B3), 5735–5770.

Le Dortz, K., B. Meyer, M. Sébrier, R. Braucher, D. Bourlès, L. Benedetti, H. Nazari, and M. Foroutan (2012), Interpreting scattered in-situ produced cosmogenic nuclide depth-profile data, *Quat. Geochronol.*, *11*, 98–115.

Maddy, D., D. Bridgland, and R. Westaway (2001), Uplift-driven valley incision and climate-controlled river terrace development in the Thames Valley, UK, *Quat. Int.*, *79*(1), 23–36.

Martschini, M., et al. (2013), AMS of ^{36}Cl with the VERA 3-MV tandem accelerator, *Nucl. Instrum. Methods Phys. Res., Sect. B*, *294*, 115–120.

Merchel, S., et al. (2011), Ultra-trace analysis of ^{36}Cl by accelerator mass spectrometry: An interlaboratory study, *Anal. Bioanal. Chem.*, *400*(9), 3125–3132.

Mitra, G. (1997), Evolution of salients in a fold-and-thrust belt: The effects of sedimentary basin geometry, strain distribution and critical taper, in *Evolution of Geological Structures in Micro- to Macro-scales*, edited by S. Sengupta, p. 59–90, Chapman and Hall, London.

Nichols, K. K., P. R. Bierman, M. Caffee, R. Finkel, and J. Larson (2005), Cosmogenically enabled sediment budgeting, *Geology*, *33*(2), 133–136.

Niedermann, S. (2002), Cosmic-ray-produced noble gases in terrestrial rocks: dating tools for surface processes, *Rev. Mineral. Geochem.*, *47*(1), 731–784.

Niedermann, S., T. Graf, and K. Marti (1993), Mass spectrometric identification of cosmic-ray-produced neon in terrestrial rocks with multiple neon components, *Earth Planet. Sci. Lett.*, *118*, 65–73.

Niedermann, S., W. Bach, and J. Erzinger (1997), Noble gas evidence for a lower mantle component in MORBs from the southern East Pacific Rise: Decoupling of helium and neon isotope systematics, *Geochim. Cosmochim. Acta*, *61*, 2697–2715.

Nishiizumi, K., M. Imamura, M. W. Caffee, J. R. Southon, R. C. Finkel, and J. McAninch (2007), Absolute calibration of ^{10}Be AMS standards, *Nucl. Instrum. Methods Phys. Res. B*, *258*(2), 403–413.

Okay, A. I., and O. Tüysüz (1999), Tethyan sutures of northern Turkey, *Mediterr. Basins: Tertiary Ext. Alpine Orogen*, *156*, 475–515.

Ouimet, W. B., K. X. Whipple, B. Crosby, J. Johnson, and T. Schildgen (2008), Epigenetic gorges in actively incising landscapes, *Earth Surf. Process. Landforms*, *33*, 1993–2009, doi:10.1002/ESP1650.

Pan, B., D. Burbank, Y. Wang, G. Wu, J. Li, and Q. Guan (2003), A 900 k.y. record of strath terrace formation during glacial-interglacial transitions in northwest China, *Geology*, *31*(11), 957–960.

Pazzaglia, F. J., and M. T. Brandon (2001), A fluvial record of long-term steady-state uplift and erosion across the Cascadia Forearc High, Western Washington State, *Am. J. Sci.*, *301*(4–5), 385–431.

Pelletier, J. D. (2010), How do pediments form?: A numerical modeling investigation with comparison to pediments in southern Arizona, USA, *Geol. Soc. Am. Bull.*, *122*(11-12), 1815–1829.

Perg, L. A., R. S. Anderson, and R. C. Finkel (2001), Use of a new ^{10}Be and ^{26}Al inventory method to date marine terraces, Santa Cruz, California, USA, *Geology*, *29*(10), 879–882.

Repka, J. L., R. S. Anderson, and R. C. Finkel (1997), Cosmogenic dating of fluvial terraces, Fremont River, Utah, *Earth Planet. Sci. Lett.*, *152*(1–4), 59–73.

Şaroğlu, F., Ö. Emre, and İ. Kuşçu (1992), Türkiye Diri Fay Haritası (Active Fault Map of Turkey), scale 1:2,000,000, one sheet. Maden Tetk. Arama Genel Müdürlüğü.

Schildgen, T. F., K. V. Hodges, K. X. Whipple, P. W. Reiners, and M. S. Pringle (2007), Uplift of the western margin of the Andean plateau revealed from canyon incision history, southern Peru, *Geology*, *35*(6), 523–526.

Schildgen, T. F., D. Cosentino, B. Bookhagen, S. Niedermann, C. Yildirim, H. Echtler, H. Wittmann, and M. R. Strecker (2012), Multi-phased uplift of the southern margin of the Central Anatolian plateau, Turkey: A record of tectonic and upper mantle processes, *Earth Planet. Sci. Lett.*, *317–318*, 85–95.

Schimmelpfennig, I., L. Benedetti, R. Finkel, R. Pik, P. H. Blard, D. Bourlès, P. Burnard, and A. Williams (2009), Sources of in-situ ^{36}Cl in basaltic rocks. Implications for calibration of production rates, *Quat. Geochronol.*, *4*(6), 441–461.

Schumm, S. A. (1977), *The Fluvial System*, 388 pp., Wiley, New York.

Şenel, M. (ed.) (2002), Türkiye Jeoloji Haritası/ Geological Map of Turkey, scale 1:500,000. Maden Tetk. Arama Genel Müdürlüğü Ankara. 19 sheets.

Şengör, A. M. C. (1995), The larger tectonic framework of the Zonguldak coasl basin in Northern Turkey: An outsider's view, in *Zonguldak Basin research wells-1*, edited by M. N. Yalçın, and G. ve Gürdal, pp. 1–26, Kozlu-K20G. TUBİTAK-MAM, GEBZE.

Şengör, A. M. C., O. Tüysüz, C. İmren, M. Sakınç, H. Eyidoğan, N. Görür, X. Le Pichon, and C. Rangin (2005), The North Anatolian Fault: A new look, *Annu. Rev. Earth Planet. Sci.*, *33*(1), 37–112.

Siame, L. L., D. L. Bourlès, M. Sébrier, O. Bellier, J. Carlos Castano, M. Araujo, M. Perez, G. M. Raisbeck, and F. Yiou (1997), Cosmogenic dating ranging from 20 to 700 ka of a series of alluvial fan surfaces affected by the El Tigre fault, Argentina, *Geology*, *25*(11), 975–978.

Stone, J. O. (2000), Air pressure and cosmogenic isotope production, *J. Geophys. Res.*, *105*(B10), 23,753–23,759.

Stone, J. O., G. L. Allan, L. K. Fifield, and R. G. Cresswell (1996), Cosmogenic chlorine-36 from calcium spallation, *Geochim. Cosmochim. Acta*, *60*(4), 679–692.

Strecker, M. R., P. Cerveny, A. L. Bloom, and D. Malizia (1989), Late Cenozoic tectonism and landscape development in the foreland of the Andes: Northern Sierras Pampeanas (26°-28°S), Argentina, *Tectonics*, *8*(3), 517–534.

Tosdal, R. M., A. H. Clark, and E. Farrar (1984), Cenozoic polyphase landscape and tectonic evolution of the Cordillera Occidental, southernmost, *Geol. Soc. Am. Bull.*, *95*(11), 1318–1332.

Tüysüz, O. (1999), Geology of the Cretaceous sedimentary basins of the Western Pontides, *Geol. J.*, *34*(1-2), 75–93.

Vandenberghe, J. (2003), Climate forcing of fluvial system development: An evolution of ideas, *Quat. Sci. Rev.*, *22*(20), 2053–2060.

Wegmann, K. W., and F. J. Pazzaglia (2002), Holocene strath terraces, climate change, and active tectonics: The Clearwater River basin, Olympic Peninsula, Washington State, *Geol. Soc. Am. Bull.*, *114*(6), 731–744.

Wegmann, K. W., and F. J. Pazzaglia (2009), Late Quaternary fluvial terraces of the Romagna and Marche Apennines, Italy: Climatic, lithologic, and tectonic controls on terrace genesis in an active orogen, *Quat. Sci. Rev.*, *28*(1–2), 137–165.

Westaway, R., M. Pringle, S. Yurtmen, T. Demir, D. Bridgland, G. Rowbotham, and D. Maddy (2004), Pliocene and Quaternary regional uplift in western Turkey: The Gediz River terrace staircase and the volcanism at Kula, *Tectonophysics*, *391*(1–4), 121–169.

Whipple, K. X., and B. J. Meade (2004), Controls on the strength of coupling among climate, erosion, and deformation in two-sided, frictional orogenic wedges at steady state, *J. Geophys. Res.*, *109*, F01011, doi:10.1029/2003JF000019.

Wobus, C., A. Heimsath, K. Whipple, and K. Hodges (2005), Active out-of-sequence thrust faulting in the central Nepalese Himalaya, *Nature*, *434*(7036), 1008–1011.

Yildirim, C., T. F. Schildgen, H. Echtler, D. Melnick, and M. R. Strecker (2011), Late Neogene and active orogenic uplift in the Central Pontides associated with the North Anatolian Fault: Implications for the northern margin of the Central Anatolian Plateau, Turkey, *Tectonics*, *30*, TC5005, doi:10.1029/2010TC002756.

Zreda, M. G., F. M. Phillips, D. Elmore, P. W. Kubik, P. Sharma, and R. I. Dorn (1991), Cosmogenic chlorine-36 production rates in terrestrial rocks, *Earth Planet. Sci. Lett.*, *105*(1–3), 94–109.

Erratum

In the originally published version of this article, the addresses of affiliations were correct but numbering of authors according to their affiliations was not. In Tables 1, 3, and 4, coordinates of three samples and digits of cosmogenic nuclide concentrations were incorrect. Although the results of the paper are correct the wrongly written coordinates and digits of concentrations may mislead the readers about the calculations. The errors have since been corrected and this version may be considered the authoritative version of record.

Corrected Affiliations

Cengiz Yildirim,[1,2,3] Taylor F. Schildgen,[3] Helmut Echtler,[2] Daniel Melnick,[3] Bodo Bookhagen,[4] Attila Çiner,[5] Samuel Niedermann,[2] Silke Merchel,[6] Martin Martschini,[7] Peter Steier,[7] and Manfred R. Strecker [3]

Corrected Table 1

Table 1. Locations, AMS Results, and Model Ages (Inheritance Is Not Corrected) of ^{10}Be Samples

Sample	Latitude (^{o}N)	Longitude (^{o}E)	Elevation (m asl)	Production Rate[a] Spallation	Production Rate[a] Muons	Quartz (g)	Be Carrier (mg)	^{10}Be/^{9}Be (x10^{-13})	^{10}Be Concentraion (104 atoms/ gSiO$_2$)	^{10}Be Model Age[b] (ka)
1	41.4075	35.0941	219	5.03	0.193	98.94	0.20	2.66±0.07	3.5±0.1	7±1
2a	41.5597	34.6714	350	5.65	0.202	114.36	0.20	39.00±0.75	44.6±0.9	81±8
5	41.6314	34.3954	508	6.50	0.213	106.77	0.19	12.77±0.22	15.5±0.3	24±2
6	41.4844	34.1255	618	7.07	0.221	106.34	0.19	24.77±0.47	30.2±0.6	43±4
7	41.4960	33.8898	776	8.08	0.233	100.44	0.20	64.65±0.91	83.9±1.2	110±10
8	41.4634	33.6730	842	8.51	0.239	113.50	0.20	43.17±0.60	51.2±0.7	178±18
10	41.4674	33.4949	903	8.88	0.243	103.18	0.20	134.70±1.00	170.5±1.3	219±23
11	41.4902	33.4740	902	9.01	0.244	86.08	0.20	148.60±3.10	226.9±4.7	304±34
12a	41.4955	33.7673	882	8.81	0.242	100.00	0.19	44.78±0.72	58.6±0.9	60±5
14a	41.2510	33.9668	1274	11.94	0.275	104.20	0.20	55.30±0.64	69.8±0.8	60±5

[a]Production rates (atoms/g/a) calculated using Lal [1991]/Stone [2000] constant production scaling for surface samples, assuming negligible shielding.
[b]^{10}Be ages were calculated using the Cronus online calculator [*Balco et al.,* 2008], assuming no surface denudation. Uncertainties are reported at the 1σ confidence level. 10Be/9Be ratio for standard = 2.85E_12.

Corrected Table 3

Table 3. Locations, AMS Results, and Model Ages (Inheritance Is Not Corrected) of ^{36}Cl Samples

Sample	Latitude (^{o}N)	Longitude (^{o}E)	Elevation (m asl)	Production Rate[a] (atoms/g*a)	36 Cl Concentration (104 atoms/g)	36Cl Model Age[b] (ka)
2b	41.5597	34.6714	350	69.2	230.6±6.6	133±13
3	41.5776	34.6571	360	709	220.4±7.0	118±12
4	41.6129	34.5552	500	78.3	640±12	438±64
9	41.4734	34.5767	931	105.9	460.4±4.6	178±20
12b	41.4955	33.7673	882	109.9	291±10	108±11

[a]^{36} Cl production rates were calculated using Stone et al. [1996] constant production scaling factor with negligible shielding.
[b]^{36}Cl ages were calculated by using Excel Add-on spreadsheet from Schimmelpfennig et al. [2009] assuming no surface denudation. Uncertainties are reported at the 1σ confidence level.

Corrected Table 4

Table 4. Locations and AMS Results of ^{10}Be Samples From Depth Profiles DA and DB

Sample	Latitude (^{o}N)	Longitude (^{o}E)	Elevation (m asl)	Depth (cm)	Production Rate[a] Spallation	Production Rate[a] Muons	Quartz	Be Carrier (mg)	^{10}Be/^{9}Be[b] (x10^{-13})	^{10}Be Concentration[b] (10^4 atoms/ g SiO^2)
DA_0	41.3933	35.1170	240	0	5.08	0.194	93.56	0.1959	n/a	n/a
DA_1	41.3933	35.1170		100	1.46	0.168	140.83	0.1907	14.27±0.32	12.91±0.29
DA_2	41.3933	35.1170		200	042	0.149	199.09	0.1939	24.46±0.55	15.91±0.36
DB_0	41.4912	33.9836	652	0	7.26	0.224	112.98	0.1942	69.72±1.60	80.07±1.83
DB_1	41.4912	33.9836		120	2.08	0.196	200.11	0.1915	44.78±0.72	28.62±0.46
DB_2	41.4912	33.9836		220	0.6	0.171	101.11	0.1919	12.31±0.20	15.62±0.25